RSC Advances

PAPER

View Article Online
View Journal | View Issue

Cite this: *RSC Adv.*, 2022, **12**, 23736

The remarkable performance of a single iridium atom supported on hematite for methane activation: a density functional theory study†

Kefale Wagaw Yizengaw,[ab] Tigist Ayalew Abay,[a] Delele Worku Ayele[c] and Jyh-Chiang Jiang *[a]

Received 10th June 2022
Accepted 13th August 2022

DOI: 10.1039/d2ra03585e

rsc.li/rsc-advances

Methane is the major component of natural gas, and it significantly contributes to global warming. In this study, we investigated methane activation on the α-Fe_2O_3(110) surface and M/α-Fe_2O_3(110) surfaces (M = Ag, Ir, Cu, or Co) using the density-functional theory (DFT) + *U* method. Our study shows that the Ir/α-Fe_2O_3(110) surface is a more effective catalyst for C–H bond activation than other catalyst surfaces. We have applied electron density difference (EDD), density of states (DOS), and Bader charge calculations to confirm the cooperative CH···O and agostic interactions between CH_4 and the Ir/α-Fe_2O_3(110) surface. To further modify the reactivity of the Ir/α-Fe_2O_3(110) surface towards methane activation, we conducted a study of the effect of oxygen vacancy (O_V) on C–H activation and CH_4 dehydrogenation. In the comparison of pristine α-Fe_2O_3(110), Ir/α-Fe_2O_3(110), and Ir/α-Fe_2O_3(110)–O_V surfaces, the Ir/α-Fe_2O_3(110)–O_V surface is the best in terms of CH_4 adsorption energy and C–H bond elongation, whereas the Ir/α-Fe_2O_3(110) surface catalyst has the lowest C–H bond activation barrier for the CH_4 molecule. The calculations indicate that the Ir/α-Fe_2O_3(110)–O_V surface could be a candidate catalyst for CH_4 dehydrogenation reactions.

1. Introduction

Methane is the major component of natural gas and a potential clean energy carrier because of its highest H to C ratio of any fossil fuel.[1–4] With the industrial revolution, methane is considered an alternative to nonrenewable petroleum resources and plays a significant role in the energy field.[5–8] Consequently, the combustion of methane leads to 25% of the global CO_2 emission, and methane itself is a greenhouse gas, which has a relative greenhouse impact of 25 times greater than CO_2. This rise in the greenhouse gas concentration, predominantly methane in the earth's atmosphere, triggered an increase in global air pollution and surface temperature.[9,10] Hence, the methane conversion to valuable commodity chemicals near its source is essential in the industry and addresses environmental concerns.

Over the decades, various strategies, including direct and indirect routes, have been developed to use methane effectively; however, the C–H bond activation under mild conditions is challenging.[10–13] The chemical products based on direct methane conversion have received significant interest in recent decades from industry and academia due to their more energy-efficient and environmental-friendliness.[14–16] The rutile IrO_2 surface has been the subject of intensive theoretical[17–19] and experimental studies,[20–22] among the different catalysts in methane conversion owing to its remarkable reactivity. In addition, much evidence endorses this superior catalytic reactivity and intrinsic electronic characteristics of the IrO_2 surface in methane activation.[23] Besides its higher reactivity, the high cost and the natural scarcity of iridium significantly limit its further development and application.

The doping of a single metal atom in metal oxide surfaces has attracted considerable interest, as it could afford precious metal thrifting and solve the ultimate goal of designing efficient and low-cost catalysts in heterogeneous catalysis.[24–28] For example, Y. Meng *et al.* demonstrated that the doping of the Pd atom improved the thermodynamic stability and catalytic performance of the Cu(111) surface towards partial oxidation of methane than the single Pd atom adsorbed surface.[28] Similarly, Guo and coworkers[29] have recently shown that Rh doped Ni(111) catalyst exhibits promising performance for coke resistance in the CH_4/CO_2 reforming reaction. Besides, the density functional theory calculations by Eisenberg and Baer have demonstrated that doping of Li atom on MgO significantly eases the hydrogen abstraction reaction from methane.[27] Furthermore, recent

[a]*Department of Chemical Engineering, National Taiwan University of Science and Technology, Taipei 106, Taiwan. E-mail: jcjiang@mail.ntust.edu.tw*

[b]*Faculty of Chemical and Food Engineering, Bahir Dar Institute of Technology, Bahir Dar University, Bahir Dar, Ethiopia*

[c]*Department of Chemistry, College of Science, Bahir Dar University, Bahir Dar, Ethiopia*

† Electronic supplementary information (ESI) available: Tables 1S–3S, Fig. 1S–8S, and POSCAR files of the initial, intermediate, and final products. See https://doi.org/10.1039/d2ra03585e

studies have described the role of single metal atom dopants in Al_2O_3 and zeolites for the activity, selectivity, stability, and regeneration capability of catalysts in propane and light alkane dehydrogenation.[30–32] Previous studies have shown that the metal oxides doped with low-valence metal atoms show better catalytic activity towards methane activation than the non-doped oxides.[33–35] Compared with other metal oxides, hematite is abundant, inexpensive, and environmentally benign. It has been widely used as a catalyst and supports catalysis because of its stability and attractive physicochemical

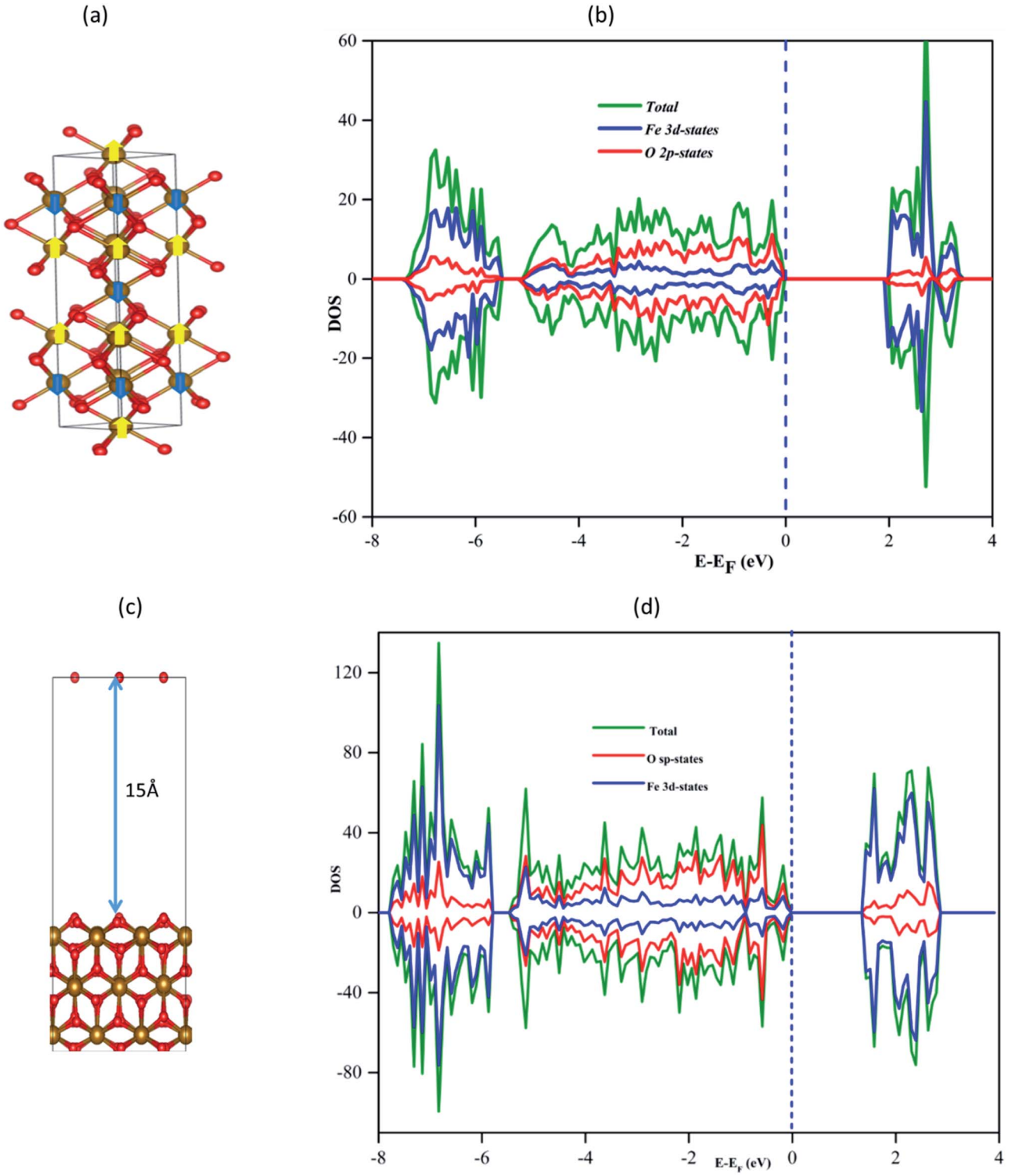

Fig. 1 (a) α-Fe_2O_3 lattice with an antiferromagnetic spin arrangement indicated; spin up by yellow and down spin by blue arrows at Fe sites (b) density of states of the bulk hematite (c) calculated optimum hematite (110) surface structure and (d) DOS of the α-Fe_2O_3(110) surface plane.

properties.[36–38] Furthermore currently researchers used iridium oxide as a catalyst for methane activation. But iridium oxide is rare earth metal oxide and it is too expensive.

Motivated by these analyses and to design the low-cost catalyst with the comparable catalytic performance of $IrO_2(110)$ surface, in this work, we designed a distinct type of different single-atom doped on hematite (α-Fe_2O_3) surface. In addition, we explored its catalytic activity towards methane adsorption and activation using density functional theory calculations. Furthermore, previous studies[39] indicate that the presence of oxygen vacancies in the metal oxide supports enhanced the methane activation; hence we also examined the effects of a single oxygen vacancy on the hematite support for C–H activation.

2. Computational details

All the spin-polarized DFT calculations were carried out using the widely used plane wave Vienna *ab initio* simulation package (VASP).[40,41] The nonlocal optB88-vdW exchange–correlation functional was used in this study, which explicitly includes the effects of van der Waals forces.[42–44] The core electrons were represented by the projector augmented wave (PAW),[45] and the energy cutoff for all the calculations was set to 500 eV based on our benchmark results. The atomic positions were optimized until the total energy converged to 10^{-4} eV, and the atomic positions were relaxed using the quasi-Newton algorithm until the x, y, and z components of the unconstrained atomic force were smaller 2×10^{-2} eV Å^{-1}. To treat the on-site Coulomb and exchange interaction of the strongly localized 3d electrons of metal atoms, here we employed the DFT + U mechanism. The DFT + U is a widely used method to describe transition metal-related studies and we conduct the benchmark calculation of the U value for each transition metal. Thus, one of the most common approaches to determine the appropriate values of U is to compare the calculated band gap for a set of U values with the experimental band gap.[46,47] As shown in Fig. 1S,† when the U value increases the band gap of the oxide also increase for all dopant case. The experimental band gaps are 0,[48] 2.18,[49] 2.85,[50] 1.6,[51] and 1.3 eV[52] for IrO_2, Fe_2O_3, CuO, CoO, and Ag_2O, respectively. Therefore, we use a combination of calculated U values derived from the fitting band gaps. For Ag, Cu, Ir, Co, and Fe, we use 5.0 eV, 4.0 eV, 0.0 eV, 3.0 eV, and 4.0 eV, respectively. Similar studies also use combination U vales for heteroatom systems.[53–57]

As shown in Fig. 2S,† the simulated XRD pattern of the α-Fe_2O_3 bulk structure shows the strongest intensity of (104) orientation, which agrees with the experimental results.[58] However, based on our surface energy calculated results for the three dominant surface planes of hematite (α-Fe_2O_3(104, 110, and 012)), α-Fe_2O_3(110) surface with the least surface energy is the most stable one, as shown in Table 1S.† Therefore, we selected the α-Fe_2O_3(110) surface.

The geometry optimization of α-Fe_2O_3 was carried out using a Monkhorst–Pack k-points scheme of $5 \times 5 \times 2$ and $2 \times 3 \times 1$ for bulk and surface calculations, respectively. For the final single-point runs for calculating the electronic properties such as DOS, a mesh of $6 \times 9 \times 1$ was used as shown in Fig. 1a. The α-Fe_2O_3 bulk structure contains iron and oxygen atoms arranged in a triangular hexagonal structure, and the calculated α-Fe_2O_3 bulk lattice parameters are ($a = b = 5.0396$ Å and $c = 13.7494$ Å) in agreement with the experimental lattice parameter values ($a = b = 5.036$ Å and $c = 13.75$ Å) and previous theoretical calculations.[59] The dopants calculated bulk lattice parameters in their bulk forms are ($a = b = c = 2.953$ $a = b = c = 4.003$, $a = b = c = 3.689$, $a = b = c = 4.194$, and $a = b = c = 4.076$ Å) for Fe, Ir, Cu, Co, and Ag, respectively, which is in agreement with the experimental lattice values.[60–62] The calculated chemical potential of the dopants is, −2.879, −6.575, −0.862, −2.003, and −1.809 for Fe, Ir, Cu, Co, and Ag, dopants, respectively, as shown in Table 2S.†

The calculated band gap of bulk α-Fe_2O_3 is 2.065 eV, as shown in Fig. 1b, which is within the experimental values (1.90–2.20 eV)[63] and similar to the previous theoretical study of 2.1 eV.[64]

The adsorption energy (E_{ads}) of the methane on the surface was calculated as

$$E_{ads} = E_{CH_4+surface} - E_{CH_4} - E_{surface}$$

where $E_{CH_4+surface}$ is the total energy of the catalyst on which methane is adsorbed, E_{CH_4} and $E_{surface}$ are the energies of the CH_4 molecule in the gas phase and the catalyst surface, respectively. We used the climbing-image nudged-elastic-band (CI-NEB)[65] method to evaluate the reaction energy barrier for methane activation, which locates the transition state (TS) structure. Vibrational frequency analyses were subsequently performed to verify the imaginary vibrational mode's uniqueness, confirming the saddle point's true nature. Charge redistributions during a surface reaction and the molecule's interaction with the surface were evaluated using the Bader charges method and partial density of states (PDOS) of atoms by considering before and after the adsorption of the CH_4 molecule.

3. Results and discussion

3.1. Surface modeling

The α-Fe_2O_3(110) surface was modeled from the optimized bulk, consisting of nine atomic layers in which the bottom three atomic layers and seven atomic layers were fixed during the structural optimization and frequency calculations, respectively. A vacuum space of 15 Å was used in the z-direction to avoid the interactions between the slabs. The α-Fe_2O_3(110) surface has three types of surface oxygen atoms: two-folded coordinated, three-folded coordinated on the top layer (denoted O_{2C} and O_{3C}, respectively), and four-folded coordinated in the subsurface (denoted as O_{4C}). The corresponding minimum distances of three differently coordinated oxygen atoms with the nearest metal atom are 1.79, 1.92, and 2.12 Å for two-, three- and four-folded coordinated oxygen atoms, respectively. The most stable surface has been chosen based on its surface energy for methane activation, as shown in Table 1S.† The relative

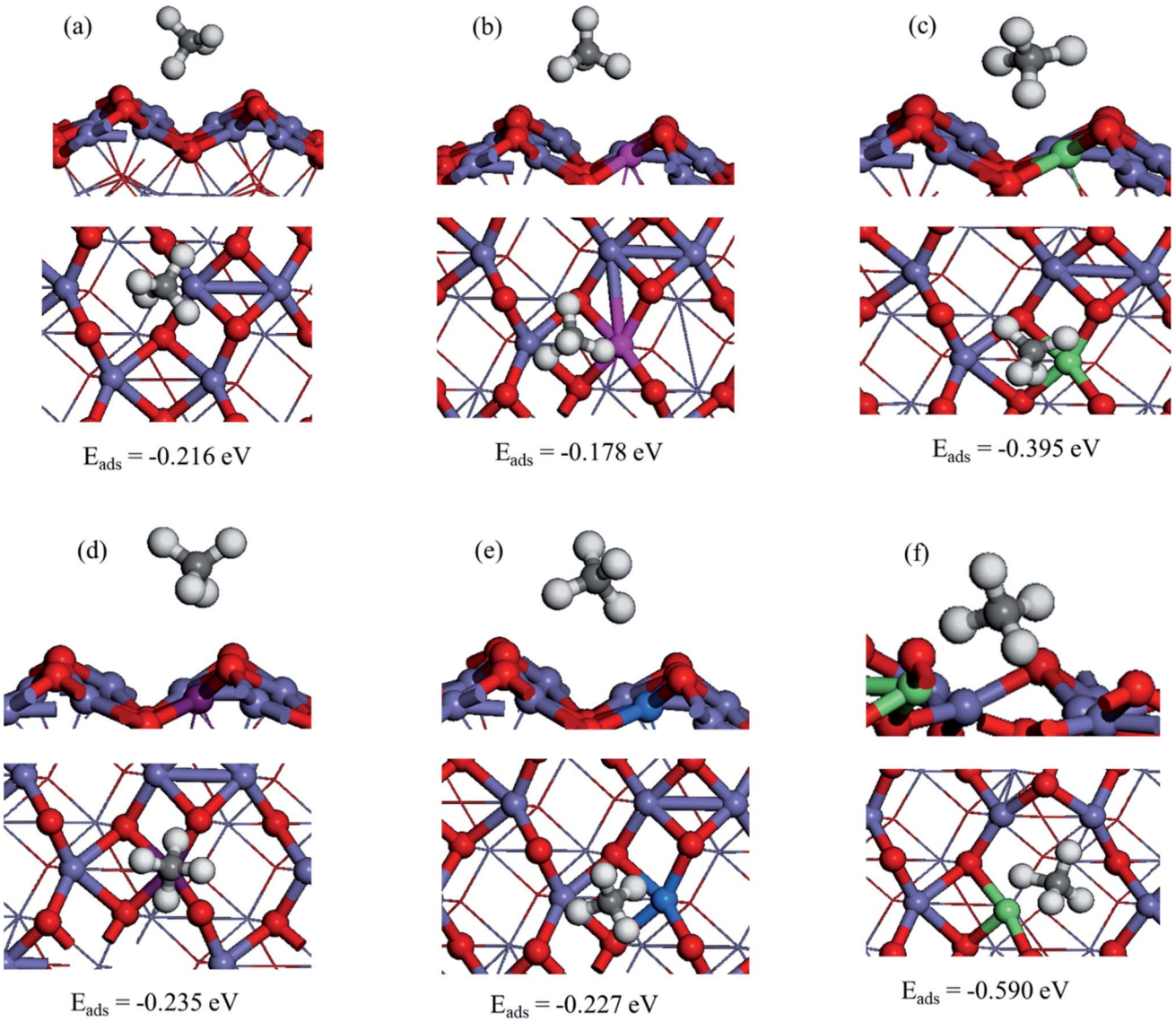

Fig. 2 Optimized structure of CH_4 adsorption on M/α-Fe_2O_3(110) surfaces: (a) α-Fe_2O_3(110), (b) Ag/α-Fe_2O_3(110), (c), Ir/α-Fe_2O_3(110), (d) Co/α-Fe_2O_3(110), (e) Cu/α-Fe_2O_3(110), and (f) Ir/α-Fe_2O_3(110)–O_V surfaces.

stability of α-Fe_2O_3(110) surface with different single metal dopants was compared by calculating formation energy as:

$$E_{form} = E_{M/Fe_2O_3} + \mu_{Fe} - E_{Fe_2O_3} - \mu_M$$

where E_{M/Fe_2O_3M} and E_{M/Fe_2O_3} are the total electronic energies of α-Fe_2O_3(110) surface after and before doping, respectively, μ_{Fe} is the chemical potential of the iron atom replaced by single-atom dopants, μ_M is the chemical potential of the dopants, and M is dopant atom (Ag, Ir, Cu, or Co). The chemical potential of the single-metal atom was assumed to be the electronic energy of a single atom in the bulk phase. Single metal atom doping site and the system geometry configuration is illustrated in Fig. 4S.†

3.2. Methane adsorption

To investigate the methane's most stable adsorption site over the pristine α-Fe_2O_3(110) surface, we considered Fe top, F–O bridge, O_{2C} top, and O_{3C} top adsorption sites, as shown in Fig. 5S.† Our results indicate that CH_4 adsorb preferentially on the Fe top of α-Fe_2O_3(110) surface with an adsorption energy of −0.211 eV by coordinating one of the C–H bonds toward the surface shown in Fig. 2a. The adsorption is relatively strong compared to those of the α-Fe_2O_3(0001) surface, on which the adsorption energy is −0.1 eV. The C⋯Fe and CH⋯O distances are 2.719 and 2.480 Å, respectively; one of the C–H bond lengths of CH_4 extended to 1.109 Å from 1.097 Å (free molecule) upon the adsorption.[66]

Further, we obtained the most stable adsorption configuration of CH_4 on different metal-doped hematite surfaces (M/α-Fe_2O_3(110)) where (M = Ag, Cu, Ir, or Co). The optimized most stable CH_4 adsorption configurations on M/α-Fe_2O_3(110) surface are shown in Fig. 2, 6S and 7S of ESI† showing the other less stable structures. The calculated adsorption energies, selective bond lengths, and distances of CH_4 adsorption on M/

Table 1 Calculated adsorption energies (E_{ads} in eV), C–H bond lengths (d_{C-H} in Å), H to surface oxygen distance ($d_{CH\cdots O}$ in Å), C to nearest metal atom distances ($d_{C\cdots M}$ in Å), activation barriers (E_a in eV), and reaction energies (ΔE in eV) for CH_4 activation on different catalyst surfaces

Surface	E_{ads}	d_{C-H}	$d_{CH\cdots O}$	$d_{C\cdots M}$	E_a	ΔE	Reference
Free CH_4 molecule	—	1.097	—	—	—	—	This study
α-Fe_2O_3(110)	−0.216	1.109	2.480	2.719	0.819	0.358	This study
Ag/α-Fe_2O_3(110)	−0.178	1.100	2.729	3.398	—	—	This study
Ir/α-Fe_2O_3(110)	−0.395	1.146	2.364	1.918	0.439	0.300	This study
Co/α-Fe_2O_3(110)	−0.235	1.099	2.701	3.797	—	—	This study
Cu/α-Fe_2O_3(110)	−0.227	1.100	3.018	3.377	—	—	This study
Ir/α-Fe_2O_3(110)–O_V	−0.590	1.182	2.805	1.794	0.585	−0.590	This study
IrO_2(110)	−0.41	1.16	2.11	—	0.300	−1.090	19
Pd/CeO_2(111)	−0.19	—	—	—	1.140	—	35
Pd/Cu(111)	−0.20	—	—	—	1.460	0.940	28
IrO_2/TiO_2(110)	−0.74	1.15	2.24	—	0.290	−1.080	68

α-Fe_2O_3(110) surfaces (M = Ag, Ir, Co, or Cu) are listed in Table 1. The CH_4 on the Ir/α-Fe_2O_3(110) surface has the largest adsorption energy and most extended C–H bond length compared to the other considered single-metal doped systems and the pristine surface. The C–H bond length is elongated to 1.146 Å from 1.097 Å (free molecule), indicating that the C–H has been significantly activated. Furthermore, the CH···O and C···Ir distances (2.364 and 1.918 Å, respectively) are much shorter than those single-metal doped systems and the pristine surface due to the more vital interaction between CH_4 and Ir/α-Fe_2O_3(110) surface.

Among the considered different single metal-doped α-Fe_2O_3(110) surfaces, Ir single atom doped α-Fe_2O_3(110) surface (Ir/α-Fe_2O_3(110)) has the CH_4 adsorption energy of −0.395 eV. As shown in Table 1, M/α-Fe_2O_3(110) surface (M = Ir) has the best results in C–H bond elongation, interaction, and CH_4 adsorption energy. The C–H bond elongation on Ir/α-Fe_2O_3(110) surface has a similar value to with IrO_2(110) surface catalyst, *i.e.*, 1.15 Å. Researchers agreed that IrO_2(110) surface catalyst has a remarkable performance for CH_4 activation.[67,68] Hence Ir/α-Fe_2O_3(110) surface catalyst has nearly similar activity to the IrO_2(110) surface in terms of C–H bond elongation. As a result, this catalyst will be one of the promising and economically feasible catalysts for CH_4 activation. Therefore, we selected the Ir/α-Fe_2O_3(110) surface catalyst for further study.

As the Ir/α-Fe_2O_3(110) surface exhibits enhanced catalytic activity toward CH_4 adsorption among the others, we further considered the presence of single oxygen vacancy on the Ir/α-Fe_2O_3(110) surface (Ir/α-Fe_2O_3(110)–O_V) and investigated the reactivity towards CH_4 activation. The oxygen vacancy formation energy O_V was calculated using the following equation:

$$E_{O_V} = E_{Ir/Fe_2O_3+O_V} + \frac{1}{2}E_{O_2} - E_{sur}$$

where $E_{Ir/Fe_2O_3+O_V}$ is the total energy of the surface with a single oxygen vacancy, E_{sur} is the electronic energy of the pure surface, and E_{O_2} is the total energy of the oxygen molecule in the gas phase. We calculated the O_V formation energy from the M/α-Fe_2O_3(110) surfaces by pulling out one oxygen atom from the top surface of the structure. From our study, the O_V formation energies of the twofold coordinated and threefold oxygen atoms from the top layer of the pristine α-Fe_2O_3(110) surface were 2.76 and 2.93 eV, respectively, similar to the previous study.[39] Similarly, O_V formation energy of the twofold coordinated and threefold coordinated oxygen atoms from the top layer of the Ir/α-Fe_2O_3(110) surface was considered. However, the structure became unstable when we created the twofold coordinated oxygen atom defect from Ir/α-Fe_2O_3(110) surface. The O_V formation energy of the threefold coordinated oxygen atoms from the top layer of the Ir/α-Fe_2O_3(110) surface was 2.55 eV. As a result, we used threefold coordinated oxygen vacancies to investigate the effect of oxygen vacancies on CH_4 adsorption; a similar method was applied in a previous study.[69]

In the same case, different adsorption sites were considered on the Ir/α-Fe_2O_3(110)–O_V surface, and each selected configuration was optimized to find a stable structure. The calculated adsorption energy for the different adsorption sites and selected geometry parameters are given in Fig. 8S.† As it has seen in Fig. 2f, it is the most stable CH_4 adsorption site on the Ir/α-Fe_2O_3(110)–O_V surface with the adsorption energy of −0.590 eV, which is much larger than that of other surfaces considered in this study. In the process of adsorption, the elongation of the activated C–H bond of CH_4 on the Ir/α-Fe_2O_3(110)–O_V surface (1.182 Å) was the greatest compared to that on other surfaces. Recent study[39] also indicates that oxygen vacancy enhanced the C–H bond activation in doped metal oxides. Ir/α-Fe_2O_3(110)–O_V surface increased the C–H bond length by 0.085 Å compared to the gaseous methane C–H bond length. The CH···O and C···Ir distances on the Ir/α-Fe_2O_3(110)–O_V surface are 2.805 and 1.794 Å, respectively. Compared to Ir/α-Fe_2O_3(110) surface, the CH···O distance becomes longer, whereas the C···Ir distance is shorter, indicating that the agostic interaction increases, whereas the CH···O interaction decreases in the case of CH_4 adsorption on Ir/α-Fe_2O_3(110)–O_V surface. The methane molecule's C–H bond elongation on the Ir/α-Fe_2O_3(110) and Ir/α-Fe_2O_3(110)–O_V surfaces was due to the CH···O and agostic interactions between C–H of CH_4 and surfaces.

3.3. Electronic structure analysis

For a detailed comparison of the electronic behavior of Ir/α-Fe_2O_3(110) and Ir/α-Fe_2O_3(110)–O_V surfaces upon CH_4 adsorption; we plotted EDD and the DOS distributions for the most

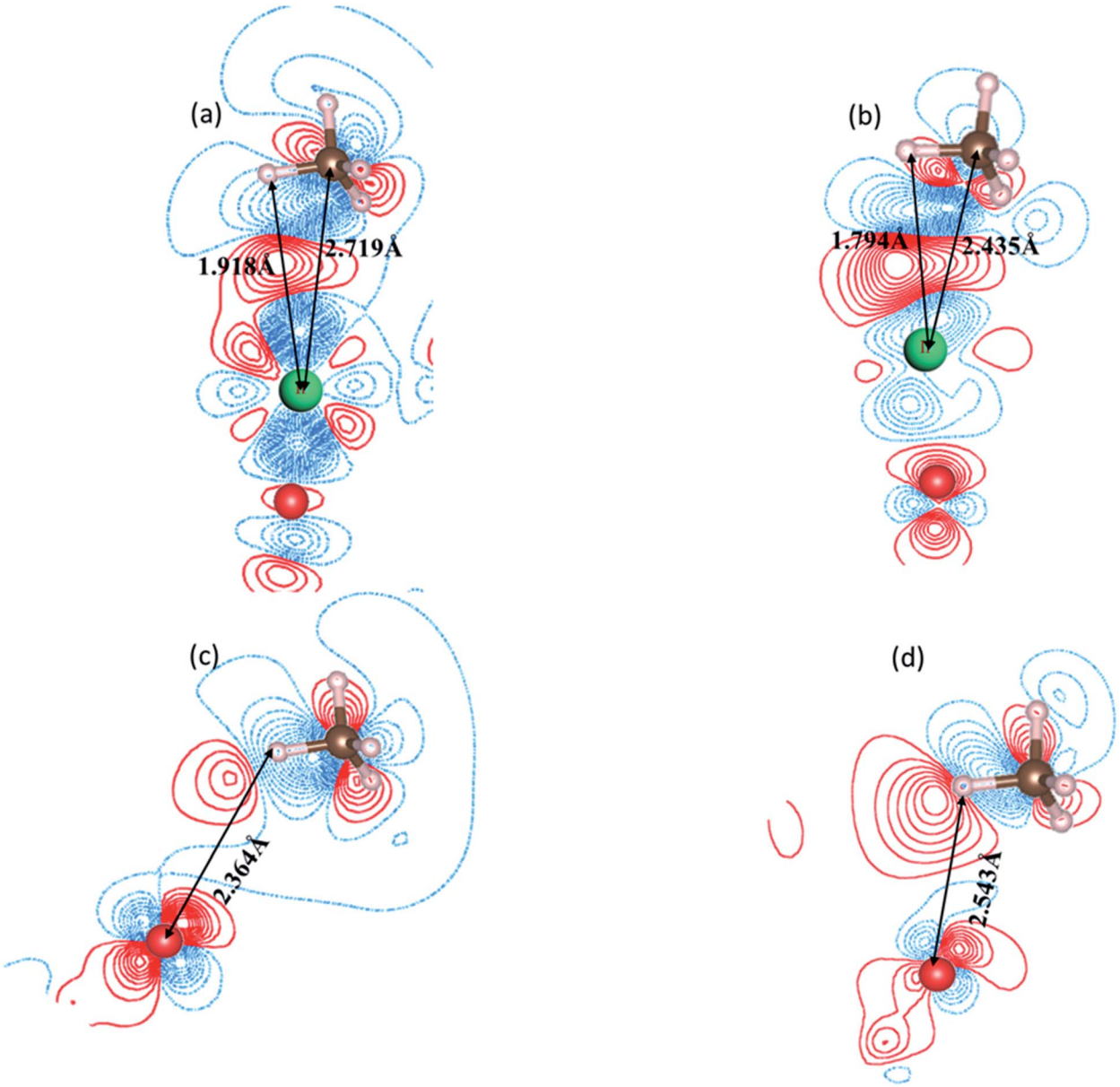

Fig. 3 2-D plots of the calculated electron density difference (EDD) for the CH_4 adsorption. (a) C–H···Ir coplanar on Ir/Fe_2O_3(110) surface, (b) C–H···Ir coplanar on Ir/Fe_2O_3(110)–O_V surface, (c) C–H···O coplanar on Ir/Fe_2O_3(110) surface and (d) C–H···O coplanar on Ir/Fe_2O_3(110)–O_V surface. The red and blue lines represent the increasing and decreasing electron densities, respectively. The isovalue is 0.002 ebohr^{-3}.

stable adsorption configurations. Fig. 3 shows the EDD contours of CH_4 adsorption on Ir/α-Fe_2O_3(110) and Ir/α-Fe_2O_3(110)–O_V surfaces with two different cutting planes (C–H···Ir and C–H···O_{cus}). As shown in Fig. 3a and b, electron accumulation between one C–H bond of methane and Ir atom on Ir/α-Fe_2O_3(110) and Ir/α-Fe_2O_3(110)–O_V surfaces were observed, which indicates the existence of agostic interaction between methane and surface. Further, as shown in Fig. 3c and d, it could be observed the electron accumulation between one of the H(C) and surface oxygen atoms on both Ir/α-Fe_2O_3(110) and Ir/α-Fe_2O_3(110)–O_V surfaces, indicating the presence of CH···O hydrogen bond between methane and the surface. The agostic interaction will make the electron transfer from methane to the surface, whereas CH···O hydrogen bonding causes the electron transfer from the surface to methane. Therefore, these two cooperative interactions between methane and the surface result in great methane adsorption energy on the Ir/α-Fe_2O_3(110) surface.[19,71] The strong interaction between methane and surface results in significant C–H bond elongation, indicating that CH_4 has significantly been activated on the Ir/α-Fe_2O_3(110) surface and Ir/α-Fe_2O_3(110)–O_V surfaces, as illustrated in Fig. 3. To understand the effect of the van der Waals force on methane adsorption, we calculated the methane adsorption energy without considering the van der Waals force correction. As shown in Table 3S,† on the surfaces of α-Fe_2O_3(110), Ir/α-Fe_2O_3(110), and Ir/α-Fe_2O_3(110)–O_V, the

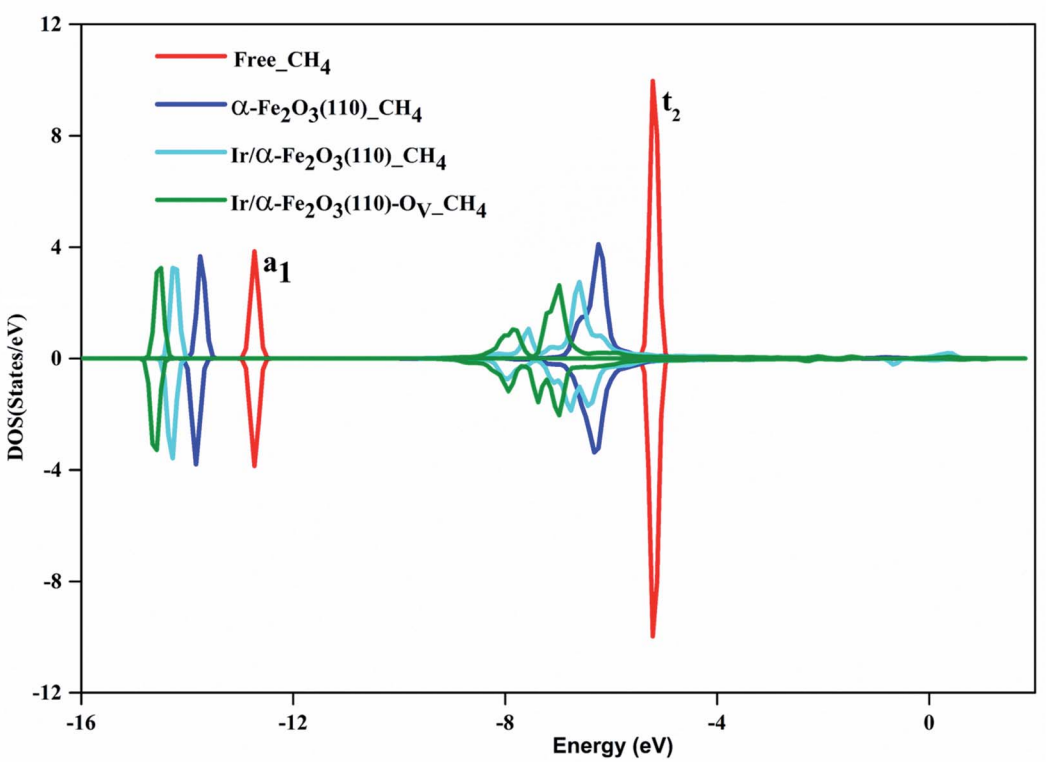

Fig. 4 The density of states of CH_4: free molecule (red line), on α-Fe_2O_3(110) (blue line), Ir/α-Fe_2O_3(110) surfaces (cyan line), and Ir/α-Fe_2O_3(110)–O_V surfaces (green line), respectively. The upper and lower panels represent spin up and spin down, respectively.

contribution of van der Waals force to methane adsorption is −0.17, −0.22, −0.32 eV, respectively. It is like the results of the literature.[70,71]

Fig. 4 shows the DOS of the CH_4 molecule before and after adsorbed on α-Fe_2O_3(110), Ir/α-Fe_2O_3(110), and Ir/α-Fe_2O_3(110)–O_V surfaces. The DOS plot of the free CH_4 molecule shows there are two peaks located at around −5.1 and −12.6 eV, which belong to the t_2 and a_1 states of CH_4 σ hybridization states, respectively. After adsorption, both states shift to lower energy regions, and the t_2 state becomes much broad. The order of amplitude of shift and broadening is α-Fe_2O_3(110) > Ir/α-Fe_2O_3(110) > Ir/α-Fe_2O_3(110)–O_V, related to adsorption energy. The interaction of CH_4 with Ir/α-Fe_2O_3(110)–O_V is the strongest, resulting in the most extensive degree of state energy downshift and broadening. The Bader charge calculation found that 0.034, 0.143, and 0.145 net electrons/charges were transferred from the CH_4 molecule to α-Fe_2O_3(110), Ir/α-Fe_2O_3(110), and Ir/α-Fe_2O_3(110)–O_V surfaces, respectively. The last two have large electrons transfer from methane to the surface, indicating that the agostic interactions are large, which causes the great C–H activation.

3.4. Methane activation

The activation of the first C–H bond is the critical and the rate-limiting step in methane conversion on most catalysts. In this work, we predominantly calculated the first dehydrogenation of CH_4 over α-Fe_2O_3(110), Ir/α-Fe_2O_3(110), and Ir/α-Fe_2O_3(110)–O_V surfaces. The calculated energy barrier and reaction energy profile for CH_4 activation over these three catalysts are illustrated in Fig. 5, and the structure of the initial state (CH_4^*), transition state (TS), and intermediate state (dis-CH_4) are given in Fig. 6. As shown in Fig. 5, the dehydrogenation barrier of the CH_4 molecule on the α-Fe_2O_3(110) surface is the largest with 0.819 eV, and the reaction energy is endothermic by 0.358 eV. The dehydrogenation barrier of the CH_4 molecule on the Ir/α-Fe_2O_3(110) surface is lowest at 0.439 eV, and reaction energy is slightly endothermic at 0.297 eV. However, the adsorption energy is −0.395 eV, smaller than the reaction barrier. Although the C–H activation barrier on Ir/α-Fe_2O_3(110)–O_V surface is 0.585 eV, which is slightly higher than that on Ir/α-Fe_2O_3(110) surface, it has larger desorption energy making the CH_4 activation reaction on the Ir/α-Fe_2O_3(110)–O_V surface can occur through a mediated mechanism and at a lower temperature. In addition, the CH_4 reaction on Ir/α-Fe_2O_3(110)–O_V surface is exothermic by 0.585 eV. Though the CH_4 adsorption energy and its C–H activation barrier over Ir/α-Fe_2O_3(110)–O_V surface compete with each other, the activation of the adsorbent on the catalyst could be proceeded by adapting the suitable reaction conditions or introducing Lewis–Brønsted acid site pairs in the catalyst.[72,73] Lercher *et al.* recently proposed the Lewis–Brønsted acid mechanism, in which the Lewis–Brønsted acid site pair dehydrogenates alkanes *via* a bifunctional mechanism that is more active than the isolated Lewis and Brønsted acid sites.[73]

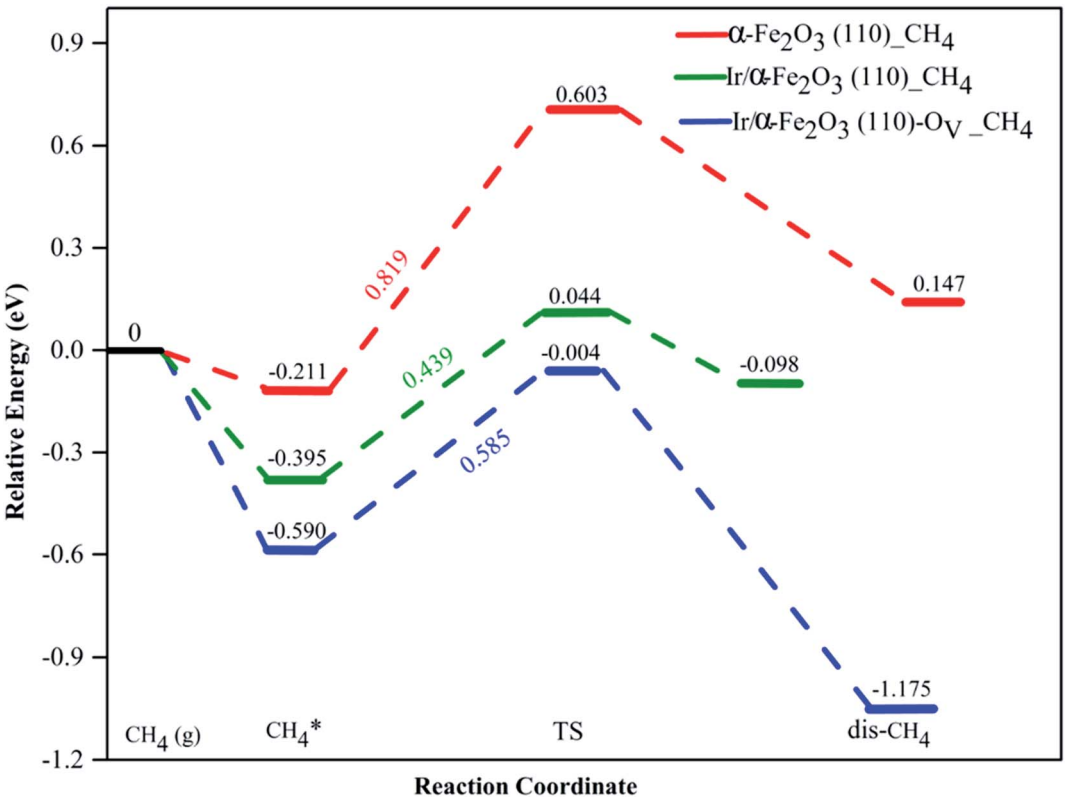

Fig. 5 Potential energy profile of CH_4 activation on α-Fe_2O_3(110) (red dash line), Ir/α-Fe_2O_3(110) (green dash line), and Ir/α-Fe_2O_3(110)–O_V surfaces (blue dash line).

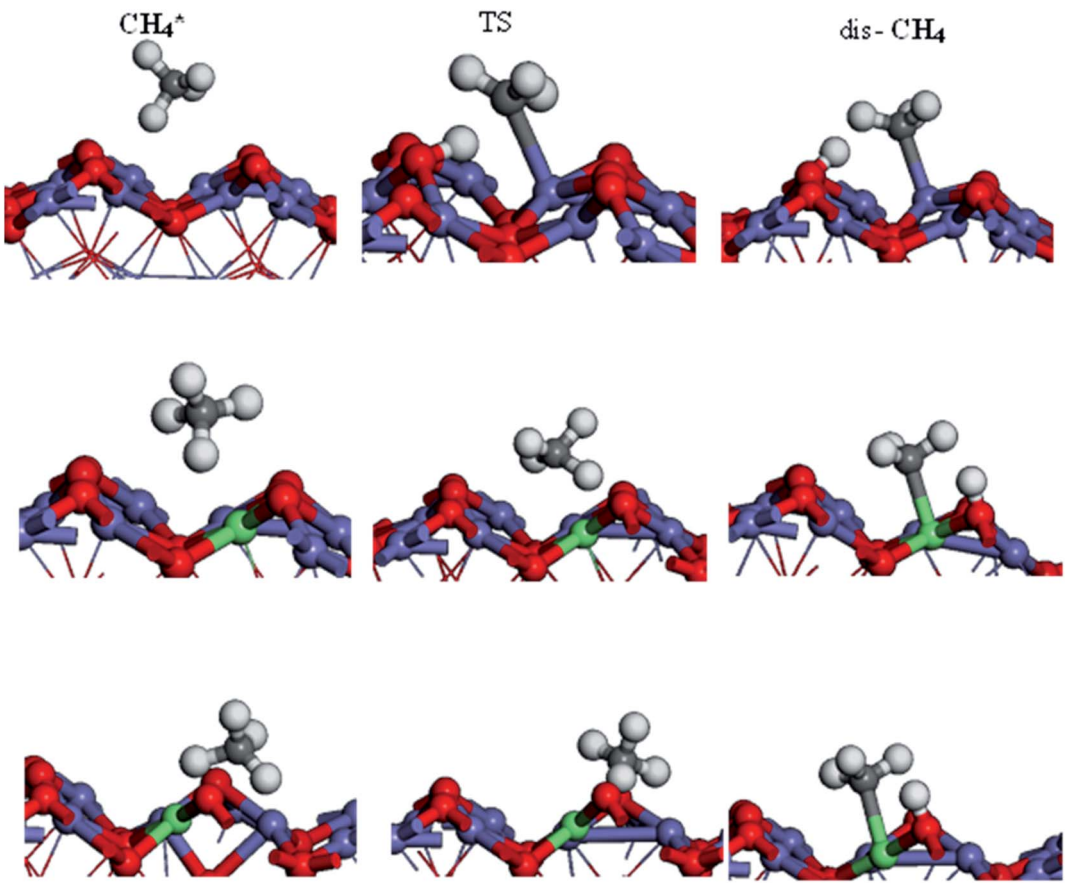

Fig. 6 Side view of initial, transition, and intermediate states of CH_4 oxidation on α-Fe_2O_3(110), Ir/α-Fe_2O_3(110), and Ir/α-Fe_2O_3(110)–O_V surfaces.

The first C–H bond activation on Ir/α-Fe_2O_3(110)–O_V surface is higher than pure IrO_2(110), and IrO_2/TiO_2(110) surfaces but much smaller compared to Pd/Cu(111) and Pd/CeO_2(111) surfaces, as shown in Table 1. After activation, the C–H bond length of the Ir/α-Fe_2O_3(110)–O_V surface is the longest, but the activation energy is higher than that of the pristine IrO_2(110) and IrO_2/TiO_2(110) surfaces. It may be due to the weaker CH···O hydrogen bonding since the CH···O distance on the Ir/α-Fe_2O_3(110)–O_V surface is longer than on the other surfaces. Likewise, the reaction energy for CH_4 activation on Ir/α-Fe_2O_3(110)–O_V surface is slightly less exothermic compared on IrO_2(110) and IrO_2/TiO_2(110) surfaces but much exothermic than on Pd/Cu(111) surface. Although compared with IrO_2(110) and IrO_2/TiO_2(110) surfaces, Ir/α-Fe_2O_3(110)–O_V surface is slightly less favorable thermodynamically and kinetically for CH_4 activation. However, this catalyst uses a relatively small amount of expensive Ir, and the activation energy is still quite low, making it a viable candidate for CH_4 activation both thermodynamically and kinetically.

To examine the relationship between activation barriers (E_a) and adsorption energies (E_{ads}) for C–H dissociation of methane on α-Fe_2O_3(110), Ir/α-Fe_2O_3(110), and Ir/α-Fe_2O_3(110)–O_V surfaces, we found that they have no linear relationship, as shown in Fig. 3S.† The bond lengths for C–H activation on α-Fe_2O_3(110), Ir/α-Fe_2O_3(110), and Ir/α-Fe_2O_3(110)–O_V surfaces are 1.408, 1.312, and 1.147 Å, respectively. It indicates that the C–H activation exists in late transition on the α-Fe_2O_3(110) surface, and early transition state on Ir/α-Fe_2O_3(110)–O_V surface, resulting in no linear relationship between adsorption energy and activation barrier.

Previous studies have shown that IrO_2 has excellent catalytic activity for methane dehydrogenation.[74,75] But methane is completely oxidized to CO_2 and H_2O.[76,77] In this study, we only considered a single metal doping and a single oxygen vacancy which is very active for methane adsorption. Cheng *et al.* studied the adsorption and dissociation of methane on ferric oxide oxygen carriers and they found that the activation barrier of C–H decreased when the surface oxygen vacancy concentration was increased from 0%–2.67%.[78] In the future, we will further investigate whether increasing the concentration of dopants and oxygen vacancies can further improve catalytic activity.

4. Conclusions

In this study, the DFT + *U* method calculations were performed to study the C–H bond activation of CH_4 molecules on the surfaces of pristine α-Fe_2O_3(110) and doped α-Fe_2O_3(110) with single-atom (Ag, Ir, Co, or Cu). From calculation results, we found that the Ir/α-Fe_2O_3(110) surface has considerable interaction with CH_4 molecules compared to other considered single-atom doped surfaces. Furthermore, we investigated the activation of CH_4 on the Ir/α-Fe_2O_3(110) surface with oxygen vacancy. EDD, DOS, and Bader charge analyses show that the coexistence of CH···O hydrogen bonding and agostic interactions between methane and surfaces results in large adsorption energies of −0.395 and −0.590 eV on Ir/α-Fe_2O_3(110) and Ir/α-Fe_2O_3(110)–O_V surfaces, respectively, and significantly elongated the length of one C–H bond on methane. Although the C–H activation barrier on Ir/α-Fe_2O_3(110)–O_V surface is slightly higher than that on Ir/α-Fe_2O_3(110) surface, it has larger desorption energy making the CH_4 activation reaction on the Ir/α-Fe_2O_3(110)–O_V surface can occur through a mediated mechanism and at a lower temperature. The calculation indicates that the first dehydrogenation of the CH_4 molecule on the Ir/α-Fe_2O_3(110)–O_V surface is thermodynamically and kinetically favorable.

Conflicts of interest

The authors declare that there is no conflict of interest.

Acknowledgements

The authors gratefully acknowledge the financial support for this work from the Ministry of Science and Technology, Taiwan (MOST 110-2113-M-011-002-MY3). The authors are also grateful to the National Center for High-Performance Computing, Taiwan, for donating computer time and facilities.

References

1 P. Tang, Q. J. Zhu, Z. X. Wu and D. Ma, *Energy Environ. Sci.*, 2014, **7**, 2580–2591.
2 P. Schwach, X. L. Pan and X. H. Bao, *Chem. Rev.*, 2017, **117**, 8497–8520.
3 E. McFarland, *Science*, 2012, **338**, 340–342.
4 R. A. Kerr, *Science*, 2010, **328**, 1624–1626.
5 E. D. Sloan, *Nature*, 2003, **426**, 353–359.
6 N. N. Xu, C. A. Coco, Y. D. Wang, T. S. Su, Y. Wang, L. W. Peng, Y. X. Zhang, Y. Y. Liu, J. L. Qiao and X. D. Zhou, *Appl. Catal., B*, 2021, **282**, 119572.
7 J. H. Lunsford, *Catal. Today*, 2000, **63**, 165–174.
8 W. Nabgan, T. A. T. Abdullah, R. Mat, B. Nabgan, Y. Gambo, M. Ibrahim, A. Ahmad, A. A. Jalil, S. Triwahyono and I. Saeh, *Renewable Sustainable Energy Rev.*, 2017, **79**, 347–357.
9 T. T. R. Karl and K. E. Trenberth, *Science*, 2003, **302**, 1719–1723.
10 D. Hu, V. V. Ordomsky and A. Y. Khodakov, *Appl. Catal., B*, 2021, **286**, 119913.
11 X. G. Guo, G. Z. Fang, G. Li, H. Ma, H. J. Fan, L. Yu, C. Ma, X. Wu, D. H. Deng, M. M. Wei, D. L. Tan, R. Si, S. Zhang, J. Q. Li, L. T. Sun, Z. C. Tang, X. L. Pan and X. H. Bao, *Science*, 2014, **344**, 616–619.
12 Y. L. Wang, P. Hu, J. Yang, Y. A. Zhu and C. Chen, *Chem. Soc. Rev.*, 2021, **50**, 4299–4358.
13 S. Q. Wu, L. Z. Wang and J. L. Zhang, *J. Photochem. Photobiol., C*, 2021, **46**, 100400.
14 X. Meng, X. Cui, N. P. Rajan, L. Yu, D. Deng and X. Bao, *Chem*, 2019, **5**, 2296–2325.
15 P. Tomkins, M. Ranocchiari and J. A. van Bokhoven, *Acc. Chem. Res.*, 2017, **50**, 418–425.
16 S. K. Li, R. Ahmed, Y. H. Yi and A. Bogaerts, *Catalysts*, 2021, **11**, 590.

17 T. L. M. Pham, E. G. Leggesse and J. C. Jiang, *Catal. Sci. Technol.*, 2015, **5**, 4064–4071.
18 T. L. M. Pham, S. Nachimuthu, J. L. Kuo and J. C. Jiang, *Appl. Catal., A*, 2017, **541**, 8–14.
19 C.-C. Wang, S. S. Siao and J.-C. Jiang, *J. Phys. Chem. C*, 2012, **116**, 6367–6370.
20 Z. Liang, T. Li, M. Kim, A. Asthagiri and J. F. Weaver, *Science*, 2017, **356**, 298–301.
21 R. Martin, M. Kim, A. Franklin, Y. X. Bian, A. Asthagiri and J. F. Weaver, *Phys. Chem. Chem. Phys.*, 2018, **20**, 29264–29273.
22 Y. X. Bian, M. Kim, T. Li, A. Asthagiri and J. F. Weaver, *J. Am. Chem. Soc.*, 2018, **140**, 2665–2672.
23 C. H. Yeh, T. M. L. Pham, S. Nachimuthu and J. C. Jiang, *ACS Catal.*, 2019, **9**, 8230–8242.
24 O. Ola and M. M. Maroto-Valer, *Appl. Catal., A*, 2015, **502**, 114–121.
25 P. D. Murzin, A. A. Murashkina, A. V. Emeline and D. W. Bahnemann, *Top. Catal.*, 2020, **64**, 817–823.
26 B. Rusinque, S. Escobedo and H. de Lasa, *Catalysts*, 2020, **10**, 74.
27 H. R. Eisenberg and R. Baer, *J. Phys. Chem. C*, 2015, **119**, 196–215.
28 Y. Meng, C. Ding, X. Gao, K. Zhang, J. Wang and Z. Li, *Appl. Surf. Sci.*, 2020, **513**, 145724.
29 F. Guo, J. Y. Ran, J. T. Niu, H. Y. Qiu and Z. L. Ou, *Int. J. Energy Res.*, 2021, **45**, 10100–10111.
30 Z. Feng, X. Liu, Y. Wang and C. Meng, *Molecules*, 2021, **26**, 2234.
31 Z. Xu, Y. Yue, X. Bao, Z. Xie and H. Zhu, *ACS Catal.*, 2019, **10**, 818–828.
32 L. Xie, R. Wang, Y. Chai, X. Weng, N. Guan and L. Li, *J. Energy Chem.*, 2021, **63**, 262–269.
33 B. Li and H. Metiu, *J. Phys. Chem. C*, 2011, **115**, 18239–18246.
34 A. D. Mayernick and M. J. Janik, *J. Phys. Chem. C*, 2008, **112**, 14955–14964.
35 Y.-Q. Su, I. A. Filot, J.-X. Liu and E. J. Hensen, *ACS Catal.*, 2018, **8**, 75–80.
36 O. Akhavan, *Appl. Surf. Sci.*, 2010, **257**, 1724–1728.
37 F. Shi, M. K. Tse, M.-M. Pohl, A. Brückner, S. Zhang and M. Beller, *Angew. Chem., Int. Ed.*, 2007, **119**, 9022–9024.
38 J. Liang, Q. H. Zhang, H. L. Wu, G. Y. Meng, Q. H. Tang and Y. Wang, *Catal. Commun.*, 2004, **5**, 665–669.
39 N. J. O'Connor, A. Jonayat, M. J. Janik and T. P. Senftle, *Nat. Catal.*, 2018, **1**, 531–539.
40 G. Kresse and J. Hafner, *Phys. Rev. B: Condens. Matter Mater. Phys.*, 1993, **47**, 558.
41 G. Kresse and J. Furthmuller, *Comput. Mater. Sci.*, 1996, **6**, 15–50.
42 J. Klimeš, D. R. Bowler and A. Michaelides, *Phys. Rev. B: Condens. Matter Mater. Phys.*, 2011, **83**, 195131.
43 J. Klimeš, D. R. Bowler and A. Michaelides, *J. Phys.: Condens. Matter*, 2009, **22**, 022201.
44 J. Klimeš and A. Michaelides, *J. Chem. Phys.*, 2012, **137**, 120901.
45 G. Kresse and D. Joubert, *Phys. Rev. B: Condens. Matter Mater. Phys.*, 1999, **59**, 1758–1775.
46 M. Arroyo-de Dompablo, A. Morales-García and M. Taravillo, *J. Chem. Phys.*, 2011, **135**, 054503.
47 C. W. Castleton, A. Lee and J. Kullgren, *J. Phys. Chem. C*, 2019, **123**, 5164–5175.
48 Y. Ping, G. Galli and W. A. Goddard III, *J. Phys. Chem. C*, 2015, **119**, 11570–11577.
49 C. Zhao, B. Li, X. Zhou, J. Chen and H. Tang, *Metals*, 2021, **11**, 424.
50 S. Sagadevan, K. Pal and Z. Z. Chowdhury, *J. Mater. Sci.: Mater. Electron.*, 2017, **28**, 12591–12597.
51 Y. Wang, H. Ge, Y. Chen, X. Meng, J. Ghanbaja, D. Horwat and J. Pierson, *Chem. Commun.*, 2018, **54**, 13949–13952.
52 L.-H. Tjeng, M. B. Meinders, J. van Elp, J. Ghijsen, G. A. Sawatzky and R. L. Johnson, *Phys. Rev. B: Condens. Matter Mater. Phys.*, 1990, **41**, 3190.
53 V. Tripkovic, H. A. Hansen and T. Vegge, *ACS Catal.*, 2017, **7**, 8558–8571.
54 Y. Tang, S. Zhao, B. Long, J.-C. Liu and J. Li, *J. Phys. Chem. C*, 2016, **120**, 17514–17526.
55 W. Li, S. G. Srinivasan, D. Salahub and T. Heine, *Phys. Chem. Chem. Phys.*, 2016, **18**, 11139–11149.
56 M. Jamal, S. S. Nishat and A. Sharif, *Chem. Phys.*, 2021, **545**, 111160.
57 M. Méndez-Galván, C. A. Celaya, O. A. Jaramillo-Quintero, J. Muniz, G. Díaz and H. A. Lara-García, *Nanoscale Adv.*, 2021, **3**, 1382–1391.
58 M. Khalil, J. J. Yu, N. Liu and R. L. Lee, *J. Nanopart. Res.*, 2014, **16**, 183–187.
59 L. Qin, Z. Cheng, M. Q. Guo, M. Y. Xu, J. A. Fan and L. S. Fan, *ACS Energy Lett.*, 2017, **2**, 70–74.
60 P. Haas, F. Tran and P. Blaha, *Phys. Rev. B: Condens. Matter Mater. Phys.*, 2009, **79**, 085104.
61 H. Eguchi, K. Tsumuraya, T. Nagano and S. Kihara, *Mater. Trans., JIM*, 1999, **40**, 1198–1204.
62 A. I. o. Physics, and D. E. Gray, *American Institute of Physics Handbook*, McGraw-Hill, 3rd edn, 1972.
63 F. Kraushofer, Z. Jakub, M. Bichler, J. Hulva, P. Drmota, M. Weinold, M. Schmid, M. Setvin, U. Diebold and P. Blaha, *J. Phys. Chem. C*, 2018, **122**, 1657–1669.
64 N. Y. Dzade, A. Roldan and N. H. de Leeuw, *Minerals*, 2014, **4**, 89–115.
65 G. Henkelman, B. P. Uberuaga and H. Jonsson, *J. Chem. Phys.*, 2000, **113**, 9901–9904.
66 J.-J. Tang and B. Liu, *J. Phys. Chem. C*, 2016, **120**, 6642–6650.
67 Y. Tsuji and K. Yoshizawa, *J. Phys. Chem. C*, 2018, **122**, 15359–15381.
68 S. Nachimuthu, H.-J. Lai, Y.-C. Chen and J.-C. Jiang, *Appl. Surf. Sci.*, 2022, **577**, 151938.
69 Y. Zhao, K. R. Yang, Z. Wang, X. Yan, S. Cao, Y. Ye, Q. Dong, X. Zhang, J. E. Thorne and L. Jin, *Proc. Natl. Acad. Sci. U. S. A.*, 2018, **115**, 2902–2907.
70 S. González, F. Viñes, J. F. García, Y. Erazo and F. Illas, *Surf. Sci.*, 2014, **625**, 64–68.
71 M. J. Tillotson, P. M. Brett, R. A. Bennett and R. Grau-Crespo, *Surf. Sci.*, 2015, **632**, 142–153.

72 X. Liu, M. Xu, L. Wan, H. Zhu, K. Yao, R. Linguerri, G. Chambaud, Y. Han and C. Meng, *ACS Catal.*, 2020, **10**, 3084–3093.
73 M. W. Schreiber, C. P. Plaisance, M. Baumgärtl, K. Reuter, A. Jentys, R. Bermejo-Deval and J. A. Lercher, *J. Am. Chem. Soc.*, 2018, **140**, 4849–4859.
74 Y. Tsuji and K. Yoshizawa, *J. Phys. Chem. C*, 2020, **124**, 17058–17072.
75 J. Xu, X.-M. Cao and P. Hu, *J. Phys. Chem. C*, 2019, **123**, 28802–28810.
76 M. Kim, A. Franklin, R. Martin, F. Feng, T. Li, Z. Liang, A. Asthagiri and J. Weaver, *J. Phys. Chem. C*, 2019, **123**, 27603–27614.
77 R. Martin, C. J. Lee, V. Mehar, M. Kim, A. Asthagiri and J. F. Weaver, *ACS Catal.*, 2022, **12**, 2840–2853.
78 Z. Cheng, L. Qin, M. Guo, J. A. Fan, D. Xu and L.-S. Fan, *Phys. Chem. Chem. Phys.*, 2016, **18**, 16423–16435.